The Astrophysical Journal Letters, 997:L4 (12pp), 2026 January 20 https://doi.org/10.3847/2041-8213/ae2ed9

JWST Spectroscopy of GRB 250702B: An Extremely Rare and Exceptionally Energetic Burst in a Dusty, Massive Galaxy at $z = 1.036$

Benjamin P. Gompertz[1,2], Andrew J. Levan[3], Tanmoy Laskar[3,4], Benjamin Schneider[5], Ashley A. Chrimes[3,6], Antonio Martin-Carrillo[7], Albert Sneppen[8,9], David O'Neill[1,2], Daniele B. Malesani[3,8,9], Peter G. Jonker[3], Eric Burns[10], Gregory Corcoran[7], Laura Cotter[7], Antonio de Ugarte Postigo[5], Massimiliano De Pasquale[11], Dimple[1,2], Rob A. J. Eyles-Ferris[12], Andrew Fruchter[13], Luca Izzo[14,15], Páll Jakobsson[16], Gavin P. Lamb[17], Jesse T. Palmerio[18], Giovanna Pugliese[19], Maria Edvige Ravasio[3,20], Andrea Saccardi[18], Ruben Salvaterra[21], Nikhil Sarin[22,23], Steve Schulze[24], Nial Tanvir[12], Isabelle Worssam[1,2], and Makenzie E. Wortley[1,2]

[1] School of Physics and Astronomy, University of Birmingham, Birmingham B15 2TT, UK; b.gompertz@bham.ac.uk
[2] Institute for Gravitational Wave Astronomy, University of Birmingham, Birmingham B15 2TT, UK
[3] Department of Astrophysics/IMAPP, Radboud University, P.O. Box 9010, 6500 GL, Nijmegen, The Netherlands
[4] Department of Physics & Astronomy, University of Utah, Salt Lake City, UT 84112, USA
[5] Aix Marseille Univ., CNRS, CNES, LAM, Marseille, France
[6] European Space Agency (ESA), European Space Research and Technology Centre (ESTEC), Keplerlaan 1, 2201 AZ Noordwijk, The Netherlands
[7] School of Physics and Centre for Space Research, University College Dublin, Belfield, Dublin 4, Ireland
[8] Niels Bohr Institute, University of Copenhagen, Jagtvej 155, 2200, Copenhagen N, Denmark
[9] The Cosmic Dawn Centre (DAWN), Denmark
[10] Department of Physics & Astronomy, Louisiana State University, Baton Rouge, LA 70803, USA
[11] University of Messina, Via F. S. D'Alcontres 31, 98166 Messina, Italy
[12] School of Physics and Astronomy, University of Leicester, University Road, Leicester, LE1 7RH, UK
[13] Space Telescope Science Institute, 3700 San Martin Drive, Baltimore, MD 21218, USA
[14] INAF, Osservatorio Astronomico di Capodimonte, Salita Moiariello 16, I-80121 Naples, Italy
[15] DARK, Niels Bohr Institute, University of Copenhagen, Jagtvej 155A, 2200 Copenhagen, Denmark
[16] Centre for Astrophysics and Cosmology, Science Institute, University of Iceland, Dunhagi 5, 107 Reykjavík, Iceland
[17] Astrophysics Research Institute, Liverpool John Moores University, IC 2 Liverpool Science Park, 146 Brownlow Hill, Liverpool, L3 5RF, UK
[18] Université Paris-Saclay, Université Paris Cité, CEA, CNRS, AIM, 91191, Gif-sur-Yvette, France
[19] Anton Pannekoek Institute of Astronomy, University of Amsterdam, Science Park 904, 1098 XH Amsterdam, The Netherlands
[20] INAF-Osservatorio Astronomico di Brera, Via Bianchi 46, I-23807, Merate (LC), Italy
[21] INAF-Istituto di Astrofisica Spaziale e Fisica Cosmica di Milano, Via A. Corti 12, 20133 Milano, Italy
[22] Kavli Institute for Cosmology, University of Cambridge, Madingley Road, CB3 0HA, UK
[23] Institute of Astronomy, University of Cambridge, Madingley Road, CB3 0HA, UK
[24] Center for Interdisciplinary Exploration and Research in Astrophysics (CIERA), Northwestern University, 1800 Sherman Avenue, Evanston, IL 60201, USA

Received 2025 September 28; revised 2025 December 2; accepted 2025 December 17; published 2026 January 12

Abstract

We present follow-up observations of the day-long, repeating gamma-ray burst (GRB) GRB 250702B with the Near Infrared Spectrograph on board the James Webb Space Telescope. Through the identification of narrow hydrogen emission lines at a consistent redshift of $z = 1.036 \pm 0.004$, we calibrate the distance scale, and therefore the energetics, of this unique extragalactic transient. At this distance, the resulting γ-ray energy release is at least $E_{\gamma,\rm iso} = 2.2 \times 10^{54}$ erg. We find no evidence for ongoing transient emission at the GRB position and exclude any accompanying supernova (SN) with a luminosity comparable to the Type Ic broad-line SN 2023lcr, though we are unable to rule out a fainter SN counterpart owing to high extinction. The inferred rate of such events, assuming at most one in the lifetime of Fermi, suggests that such bursts are very rare, with volumetric rates over 1000 times lower than normal high-luminosity long GRBs and $>10^5$ times lower than core-collapse SNe, when corrected for beaming. Furthermore, we find that the host galaxy is unique among GRB host galaxies and extremely rare in the general galaxy population, being extremely large and dusty and with high stellar mass. The identification of such an exotic GRB in such an unusual galaxy raises the possibility that the environment was important in the progenitor channel creating GRB 250702B.

Unified Astronomy Thesaurus concepts: Gamma-ray bursts (629); High energy astrophysics (739); Galaxies (573)

1. Introduction

Gamma-ray bursts (GRBs) are extremely high energy explosive transients that are generally thought to be produced by processes internal to relativistic jets launched by either the collapse of very massive stars at the ends of their lives or the merging of compact object binaries, predominantly (or possibly exclusively) neutron stars. Their gamma-ray emission is observed to be remarkably diverse, perhaps reflecting the disparate properties and environments of their stellar progenitors combined with the complex physics of jet launch, propagation, and radiation. Broadly, GRBs with durations of greater than 2 s are believed to originate from stellar collapse (termed "collapsars") thanks to their consistent association with broad-lined stripped-envelope (Type Ic-BL) supernovae (SNe; e.g., J. Hjorth et al. 2003; K. Z. Stanek et al. 2003; Z. Cano et al. 2017), though notable exceptions to this duration-based dichotomy have emerged (J. P. U. Fynbo et al. 2006; A. Gal-Yam et al. 2006;

N. Gehrels et al. 2006; J. C. Rastinejad et al. 2022; E. Troja et al. 2022; B. P. Gompertz et al. 2023; A. J. Levan et al. 2024; Y.-H. Yang et al. 2024). Collapsar GRBs have typical durations of tens to hundreds of seconds in gamma-ray emission, though rare examples of "ultralong" GRBs with gamma-ray durations of thousands to tens of thousands of seconds have been observed (Y. Y. Tikhomirova & B. E. Stern 2005; B. Gendre et al. 2013; A. J. Levan et al. 2014).

Despite this diversity, the recent identification of GRB 250702B as an extragalactic transient (A. J. Levan et al. 2025) has confirmed the burst as a truly singular event in the GRB population. Unlike all previous examples, GRB 250702B exhibited repeating structure, triggering the Fermi Gamma-ray Burst Monitor (GBM; C. Meegan et al. 2009) three times on 2025 July 2 (initially identified as GRB 250702B, GRB 250702D, and GRB 250702E; E. Neights et al. 2025), while prior X-ray emission from the same position was reported by the Einstein Probe (EP; H. Q. Cheng et al. 2025) starting on 2025 July 1. GRBs have never been seen to repeat on these timescales, and the isolated "islands" of gamma-ray emission are unlike anything previously seen in even the ultralong class of bursts (though separations of spikes on the order of kiloseconds have been observed; see, e.g., F. J. Virgili et al. 2013).

Indeed, due to the peculiarity of the burst, the off-nuclear position of the transient on its host galaxy, and the identification of a possible periodicity in the gamma-ray triggers, A. J. Levan et al. (2025) suggested that GRB 250702B may have instead arisen from the tidal disruption event (TDE) of a white dwarf around an intermediate-mass black hole (IMBH). A TDE origin was also proposed by G. Oganesyan et al. (2025). Jetted, or relativistic, TDEs have previously been observed with properties similar to GRBs: an initial strong burst of gamma rays (though with durations far in excess of those typical for GRBs), followed by a fading, multiwavelength X-ray-to-radio counterpart (D. N. Burrows et al. 2011; S. B. Cenko et al. 2012; D. R. Pasham et al. 2015; A. J. Levan et al. 2016; V. Mangano et al. 2016). The spectral energy distributions (SEDs) of relativistic TDEs have also shown them to be powered by a combination of thermal and synchrotron emission and are akin to those of GRBs (I. Andreoni et al. 2022; D. R. Pasham et al. 2023). In their modeling, A. J. Levan et al. (2025) concluded that the X-ray, near-infrared (NIR), and radio afterglow following GRB 250702B was consistent with more typical GRBs if the redshift of the source was $z \sim 0.3$ but may be more consistent with the luminosity (if not the decay rate) of relativistic TDEs at higher z. This underscores the importance of having a measured distance with which to estimate the energy release and evaluate potential progenitors.

Here we report on follow-up observations of GRB 250702B with the Near-Infrared Spectrograph (NIRSpec) on board the James Webb Space Telescope (JWST). We measure the redshift of the burst to be $z = 1.036 \pm 0.004$, and we discuss the resultant implications for the energetics. We also provide limits on an accompanying Type Ic-BL SN, which would be expected for a collapsar progenitor, and discuss our constraints on TDE progenitors. Finally, we analyze the properties of the host galaxy of GRB 250702B and discuss how this contextualizes the transient. This Letter is organized as follows: In Section 2 we outline our observations and derive a redshift for the burst. We place limits on transient counterparts in Section 3. The properties of the host galaxy are presented in Section 4. We discuss the implications of our findings in Section 5 and summarize our final conclusions in Section 6. We assume a cosmology of $H_0 = 69.6\,\mathrm{km\,s^{-1}}$, $\Omega_M = 0.286$, and $\Omega_{\mathrm{vac}} = 0.714$ (C. L. Bennett et al. 2014) throughout.

2. Observations and Redshift Determination

We observed the position of the NIR counterpart to GRB 250702B (A. J. Levan et al. 2025) at 03:12:28 UTC on 2025 August 23, 51.6 days after the Fermi trigger GRB 250702D under program GO 9254 (PI: Gompertz) with the NIRSpec unfiltered prism and $0\farcs4$ S400A1 fixed slit for an effective exposure time of 1.7 hr. We utilize the standard level 3 pipeline products from the Mikulski Archive for Space Telescopes (MAST) in our analysis. The specific observations analyzed can be accessed via doi:10.17909/4fqj-kr65.

We also observed GRB 250702B with the Enhanced Resolution Imager and Spectrograph (ERIS) mounted on Unit Telescope 4 (Yepun) of the Very Large Telescope (VLT) at Cerro Paranal Observatory, Chile. Observations were taken with the Near Infrared Camera System (NIX) starting at 00:46:25 UTC on 2025 August 23 (51.5 days after the Fermi/GBM trigger) under program 114.27PZ (PIs: Malesani, Vergani, Tanvir) with the K_s filter. The ERIS/NIX images were processed using the ESO REFLEX pipeline (W. Freudling et al. 2013), which applies detector-level calibrations, flat-fielding, and sky subtraction. From the individual reduced frames, we performed our own stacking to improve the background subtraction and enhanced the final image quality.

2.1. 1D Spectral Analysis

We deredden the 1D spectrum for a Milky Way extinction of $A_V = 0.83$ along the line of sight (E. F. Schlafly & D. P. Finkbeiner 2011) using the EXTINCTION Python package[25] and a J. A. Cardelli et al. (1989) extinction law with $R_v = 3.1$. The corrected spectrum still exhibits a very red continuum;[26] this is consistent with the high host A_V inferred by A. J. Levan et al. (2025), although their solution was for an assumed $z \approx 0.16$. A single high-significance emission line is seen at a wavelength of $\lambda_{\mathrm{obs}} \approx 3.8\,\mu$m, along with other lower-significance line candidates, most notably at $\lambda_{\mathrm{obs}} \approx 1.3\,\mu$m. Due to the paucity of available lines, we employ template matching to constrain the possible space of redshift solutions. Comparing with the NIRSpec spectrum of the host galaxy of GRB 240825A[27] ($z = 0.659$; A. Martin-Carrillo et al. 2024), we identify the high-significance line at $\lambda_{\mathrm{obs}} \approx 3.8\,\mu$m in the JWST spectrum of GRB 250702B to be most likely due to Paα at a redshift of $z \approx 1.03$. At this redshift, the 1.3 μm line is consistent with Hα, and the continuum shape also appears congruent with that of the template. In addition, by comparison with GRB 240825A, we identify a possible emission line at $\lambda_{\mathrm{obs}} \approx 4.4\,\mu$m, which would be consistent with Brγ at $z \approx 1.03$. Additional Pa series emission lines can be seen in the GRB 240825A spectrum, Paβ ($\lambda_{\mathrm{rest}} = 1.2818\,\mu$m), Pa$\gamma$ ($\lambda_{\mathrm{rest}} = 1.0938\,\mu$m), and Pa$\epsilon$ ($\lambda_{\mathrm{rest}} = 0.9546\,\mu$m), but are not seen in GRB 250702B. This can in part be explained by their

---

[25] https://extinction.readthedocs.io/en/latest/index.html

[26] Fitting the 1.5–2.5 μm region with a power-law model yields $\beta_\lambda \approx 3$ (for $F_\lambda \propto \lambda^\beta$), corresponding to $F_\nu \propto \nu^{-5}$.

[27] Also taken under program GO 9254. We extract a spectrum at a position offset from the GRB and deredden it using the same method as above but for $A_V = 0.165$ (E. F. Schlafly & D. P. Finkbeiner 2011). A full analysis of this GRB will be published in B. Schneider et al. (2025, in preparation).

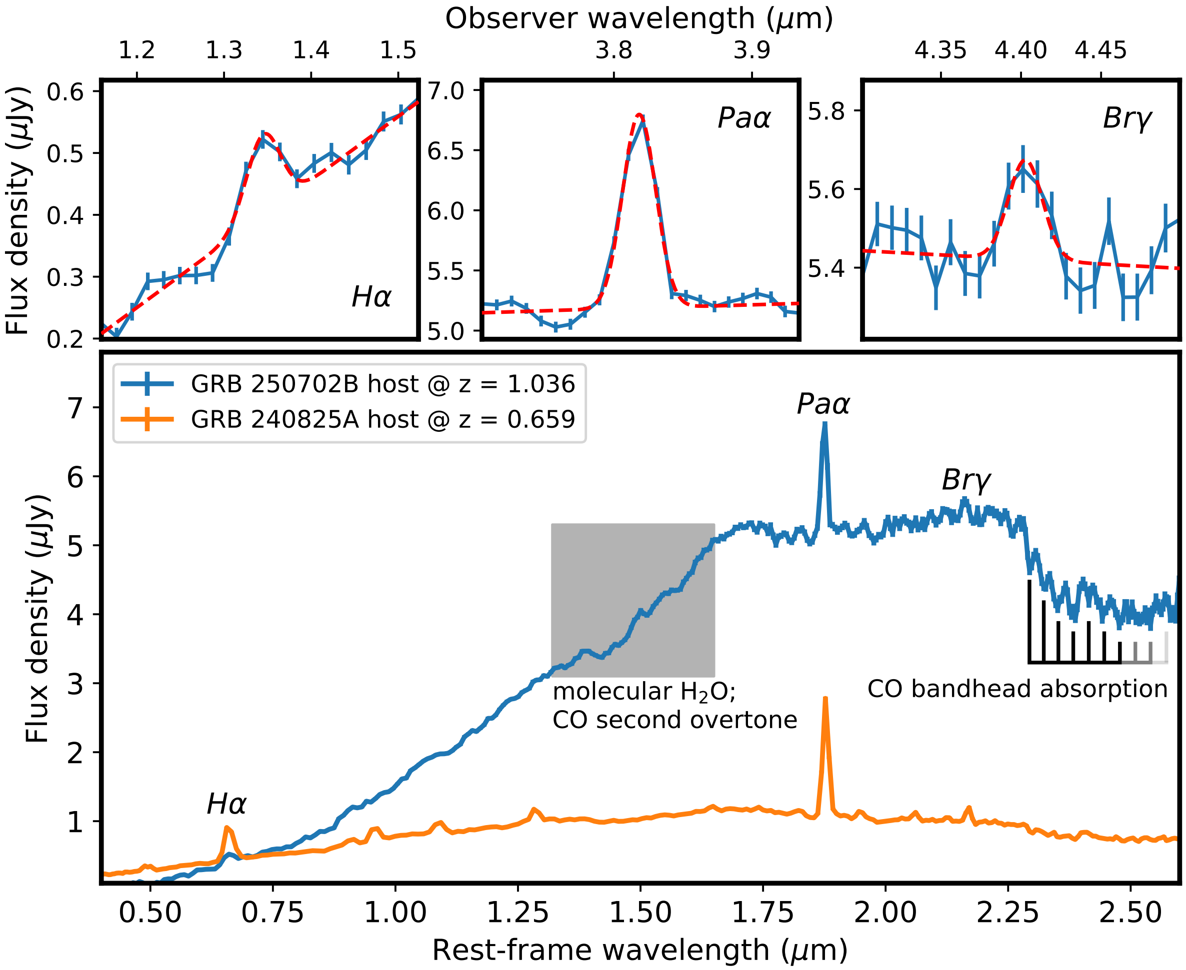

Figure 1. Rest-frame 1D spectrum (bottom panel) of GRB 250702B (blue) at the best-fit redshift of $z = 1.036$, compared to an off-transient (host galaxy) spectrum of GRB 240825A (orange) at $z = 0.659$ (A. Martin-Carrillo et al. 2024). The high-significance Paα, moderate-significance Hα, and low-significance Brγ lines are marked,and their fits are shown in the top panels. A sharp drop-off in flux is seen redward of ∼2.25 μm in the rest frame, likely due to CO band-head absorption. The expected wavelengths of individual band-head components (CO 2–0 through CO 11–9) are indicated in progressively lighter shades. Broad absorption features are also identified between 1.3 and 1.6 μm, consistent with expectations of absorption from molecular H_2O and second-overtone CO.

intrinsic faintness, but it may also suggest that a nonnegligible fraction of the Paα flux is coming from a more heavily obscured region than the Hα emission.

The rest-frame spectrum of GRB 250702B, along with the GRB 240825A template, is shown in Figure 1, with the above line identifications marked. We note a very strong drop-off in flux at the red end of the spectrum, starting at around 4.5 μm in the observer frame. Numerous low-significance features are visible in this region at wavelengths that closely match expectations for the CO first-overtone absorption band head (A. Mármol-Queraltó et al. 2008). We also identify possible broad absorption features in the region between 1.3 and 1.6 μm in the rest frame, consistent with expectations for molecular H_2O absorption (e.g., A. Lançon & P. R. Wood 2000) and second-overtone CO absorption (e.g., E. D. Tenenbaum et al. 2005). These are marked in Figure 1. The implications of these features are discussed in Section 4.

To constrain the redshift and the strength and significance of the narrow spectral lines more precisely, we fit the line candidates with Gaussian profiles. First, we isolate arbitrary wavelength regions around the line candidates and fit each with a simple Gaussian to estimate line centroid locations (m) and widths (σ). We then extract a region of 10σ on either side of the line centroid and fit each line with a Gaussian + 1D polynomial model to separate out the underlying continuum using the ASTROPY.MODELING package and the Levenberg–Marquardt least-squares fitting algorithm. The fit results are presented in Table 1. Line detection significances are given as the ratio of the integrated fluxes to their corresponding measurement errors. Fitting the derived line centroids to their expected rest values in vacuum yields a redshift of $z = 1.036 \pm 0.001$ (however, see Section 2.2 for an additional source of uncertainty in this measurement). Assuming an intrinsic case B line ratio of Paα to Hα of 0.122 (corresponding to an electron temperature $T_e \approx 10^4$ K and density $n_e \approx 10^{-2}$–10^4 cm^{-3}) along with $R_v = 3.1$ and a J. A. Cardelli et al. (1989) extinction law, the observed fluxes of these two line candidates in the integrated spectrum imply an intrinsic extinction of $A_V = 3.4 \pm 0.4$ mag from the host galaxy. We note that an unmodeled contribution to the Hα line (e.g., from blended N II emission) would result in the derived A_V values reported here being underestimated. Such blending may also help explain the large σ derived for the Hα line in Table 1.

2.2. 2D Spectral Analysis

To isolate potential light from the transient from that of the underlying galaxy, we perform a spatially resolved study by

Table 1
Line Identifications and Gaussian Fit Results

Feature	$\lambda_{\rm obs}$ (μm)	$\lambda_{\rm rest}$ (μm)	σ (nm)	Integrated Flux (Fit) (10^{-18} erg s^{-1} cm^{-2})	Integrated Flux (Fixed) (10^{-18} erg s^{-1} cm^{-2})	S/N
Hα	1.345 ± 0.003	0.656	19.5 ± 3.3	10.5 ± 2.30	2.28 ± 0.35	4.5
Paα	3.818 ± 0.001	1.875	12.0 ± 0.7	9.94 ± 0.75	9.94 ± 0.75	13.2
Brγ	4.403 ± 0.003	2.166	10.5 ± 3.2	1.01 ± 0.41	1.33 ± 0.36	2.5

Note. Integrated fluxes (corrected for Galactic extinction) are presented for the value of σ found for each line (fit), and with all line widths fixed in velocity space to the Paα value (fixed) to minimize flux uncertainties in the less significant lines. The identified lines are consistent with a redshift of $z = 1.036 \pm 0.001$.

extracting spectra along individual rows near the center of the slit (pixel rows 30–35) with sufficient signal via the `extract1d` tool in the JWST pipeline. We show the resulting output, along with its correspondence to the host, in Figure 2. We correct each of these spectra for Galactic extinction as above, and we fit the three atomic H spectral features identified above (Hα, Paα, and Brγ) with Gaussian models using a similar procedure to that in Section 2.1. We fix the width of all three features to be the same in a given spectrum, but we allow the fluxes (and the underlying continuum), as well as the redshift, to vary across the six spectra. In each case, we use the flux ratio of Paα to Hα to estimate A_V. Finally, we convert the inferred redshift from each spectrum to a velocity relative to $z = 1.036$ inferred from the integrated spectrum (Section 2.1) and present the results in Table 2.

The inferred central velocity of the spectral lines shifts monotonically from ≈850 to ≈−2400 km s^{-1} over the six pixel rows. At a redshift of $z = 1.036$, the NIRSpec pixel scale of $0\farcs1$ pixel^{-1} corresponds to a spatial resolution of 0.82 kpc pixel^{-1}. If real, this velocity structure would imply an improbably large enclosed mass of $M \approx 10^{12}(v/10^3\ {\rm km\ s^{-1}})^2(R/4.9\ {\rm kpc})\ M_\odot$. Instead, we suggest that this signature is the result of a spatially extended emission feature in the galaxy that is misaligned with the spatial direction of the slit (see Figure 2). Since the width of the NIRSpec point-spread function (PSF; $\approx 0\farcs1$) is less than the width of the employed slit (S400A1; $0\farcs4$), such a misalignment would cause a shift in the line centroid along the dispersion direction. This correlation between source placement in the slit and inferred velocity is an additional source of instrumental systematic uncertainty in the redshift measurement. To account for this effect, we include the standard deviation of the redshift measurements in the per-pixel spectra ($\sigma_z = 0.004$) in quadrature with our redshift uncertainty, giving a final redshift of $z = 1.036 \pm 0.004$.

We similarly note trends in the derived A_V values along the spatial direction, although the standard deviation of the six A_V values ($\sigma_{A_V} = 0.4$ mag) is consistent with the mean measurement uncertainty ($\bar{\sigma}_{A_V} = 0.4$). The mean $A_V = 3.6$ across the six pixels is consistent at $<1\sigma$ with A_V derived from the integrated light spectrum (Section 2.1). Thus, while there is a hint that A_V varies across the galaxy, the effect does not appear to be statistically significant.

3. Transient Properties and Limits

3.1. Afterglow Modeling

We investigate the energetics of the multiwavelength counterpart of GRB 250702B by updating the afterglow model of A. J. Levan et al. (2025), utilizing the same dataset but now fixing $z = 1.036$. We run 512 Markov Chain Monte Carlo chains for 2000 steps using EMCEE (D. Foreman-Mackey et al. 2013), discarding the first 20 steps as burn-in. Our best-fit light curves are visually indistinguishable from those in A. J. Levan et al. (2025) and are not plotted here, but we summarize our results in Figure 3. At this redshift, we infer a very large afterglow isotropic-equivalent kinetic energy of $E_{K,{\rm iso}} \approx 8 \times 10^{54}$ erg and acknowledge that this parameter is up against our prior of $E_{K,{\rm iso}} < 10^{55}$ erg. However, we stress that the paucity of constraints from the data (e.g., unobserved synchrotron self-absorption and cooling breaks; A. J. Levan et al. 2025) implies degeneracies in this model (Figure 3). An anticorrelation between $E_{K,{\rm iso}}$ and the jet break time ($t_{\rm jet}$) in this model results in a somewhat constrained, very narrow opening angle of $\theta_{\rm jet} \approx 0\fdg5$, similar to the value derived in A. J. Levan et al. (2025). The corresponding beaming-corrected kinetic energy of $E_K \approx 3 \times 10^{50}$ erg remains consistent with typical values inferred for long-duration GRBs (e.g., T. Laskar et al. 2015). This model requires ≈5.8 mag of visual extinction along the line of sight to the transient. Although lower[28] than the value ($A_V \approx 11.6$ mag) reported in A. J. Levan et al. (2025), this relatively high value is nevertheless demanded[29] by the very red NIR color of the afterglow. This A_V is higher than the host-averaged A_V inferred from the JWST spectrum ($A_V = 3.4 \pm 0.4$ mag; Section 2), but such a disparity is not atypical for long-duration GRBs (e.g., G. Schroeder et al. 2022). Finally, we confirm that there is a negligible ($\lesssim 1\%$) contribution at 51.6 days from the afterglow to the observed JWST spectrum at all wavelengths in this model.

3.2. Supernova Limits

In the standard collapsar scenario, we expect the emergence of a Type Ic-BL SN, peaking on a timescale of ∼2 weeks in the rest frame (e.g., Z. Cano et al. 2017). The detection or exclusion of an SN therefore has valuable implications for the progenitor of GRB 250702B. At the derived redshift of $z = 1.036$, our NIRSpec observations were taken around 25.5 rest-frame days after collapse, or around 11 rest-frame days after the expected peak of an accompanying SN.

We use SN 2023lcr as the template for our expected SN counterpart. This has several advantages as a comparison object: It is a confirmed Type Ic-BL SN and was detected with NIRSpec (DDT program 4554; PI: Martin-Carrillo) at an almost identical rest-frame phase (27 days;

---

[28] The lower A_V is expected at the higher redshift employed here, since the rest-frame wavelengths sampled by the observed NIR bands are correspondingly bluer.

[29] From the VLT observations at $\delta t \approx 1.6$ days, $H - K \approx 1.5$ AB mag. For a Milky Way extinction curve at $z = 1.036$, this constrains $A_V \approx (6.8 + 1.4\beta)$ mag ≈ 5.9 mag with $\beta \sim (1 - p)/2 \approx -0.55$ for $p \approx 2.2$, consistent with the estimates from our model (Figure 3).

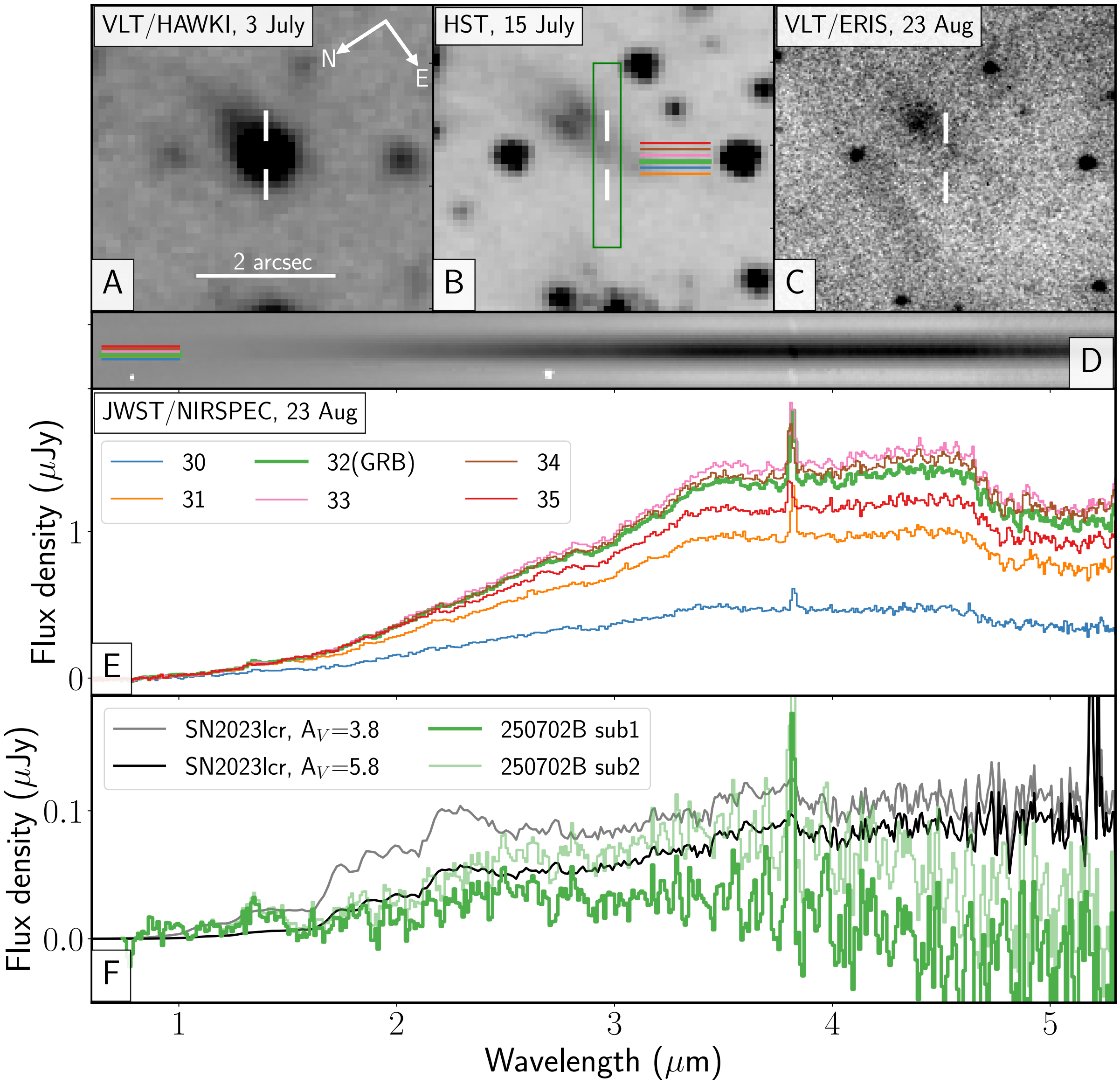

Figure 2. Spatially resolved properties of the GRB 250702B host galaxy, and SN limits. Panels (a)–(c) show imaging of the source location from July to August using the VLT and HST (A. J. Levan et al. 2025). The location of the slit is shown in panel (b), along with lines indicating the physical locations that correspond to each row in the extracted spectrum. The row containing the GRB is shown in green (row 32), and the resulting 2D spectrum is shown in panel (d). Panel (e) shows the 1D spectrum (not corrected for host or Galactic extinction) extracted from each row. The spectral shape is generally very similar in each row, with no evidence for additional emission components at the GRB location. We demonstrate this in panel (f), where we subtract a host galaxy spectrum (row 34) from that at the GRB location. Depending on the normalization of the subtraction, it is possible to have near-zero flux (sub1), or a faint component that is essentially a copy of the host galaxy spectrum (sub2). We also plot SN 2023lcr as it would appear with $A_V = 3.8$ and $A_V = 5.8$, corresponding to the inferred extinction at the burst location from the row-by-row spectral extraction (Table 2) and afterglow modeling (Section 3.1), respectively. In the lower-extinction scenario the absence of broad features can exclude SN emission to factors of 2–3 fainter than SN 2023lcr. In the higher-extinction scenario it is not possible to place meaningful constraints.

A. Martin-Carrillo et al. 2023) and an almost identical redshift ($z = 1.0272$; D. A. Perley et al. 2023). Its spectrum[30] is shown alongside the line-by-line pixel extractions (Section 2.2) in Figure 2. GRB 250702B was covered by pixel row 32, though the PSF of 0.″1 closely matches the pixel size, so transient light may also be found in adjacent rows. It is immediately apparent that no bright SN resembling SN 2023lcr is present in any of the spectra, though it is unclear whether one is absent or just extincted by dust along the line of sight.

To place limits on the presence of any SN, we must first attempt to remove the host galaxy light. Although the host spectral shape is similar across all wavelengths, there are subtle differences. We therefore chose to use pixel 34 as a subtraction template, since it is the closest match to pixel 32 in the red (where SN contribution should be smallest). It is sufficiently far from the transient to have minimal contamination and is also the brightest pixel in the galaxy while being the most comparable phenomenologically. We scale the spectra to match in the 4–4.5 μm region and then subtract, with the resulting subtraction shown in Figure 2.

For comparison, we also extract the SN 2023lcr spectrum row by row to obtain an appropriate comparison in flux space. In the case of SN 2023lcr, there is minimal host galaxy

---

[30] This spectrum was extracted from the single row of pixels that contains the SN for a more direct comparison with the GRB 250702B spectra. A full analysis of SN 2023lcr will be published in A. Martin-Carrillo et al. (2025, in preparation).

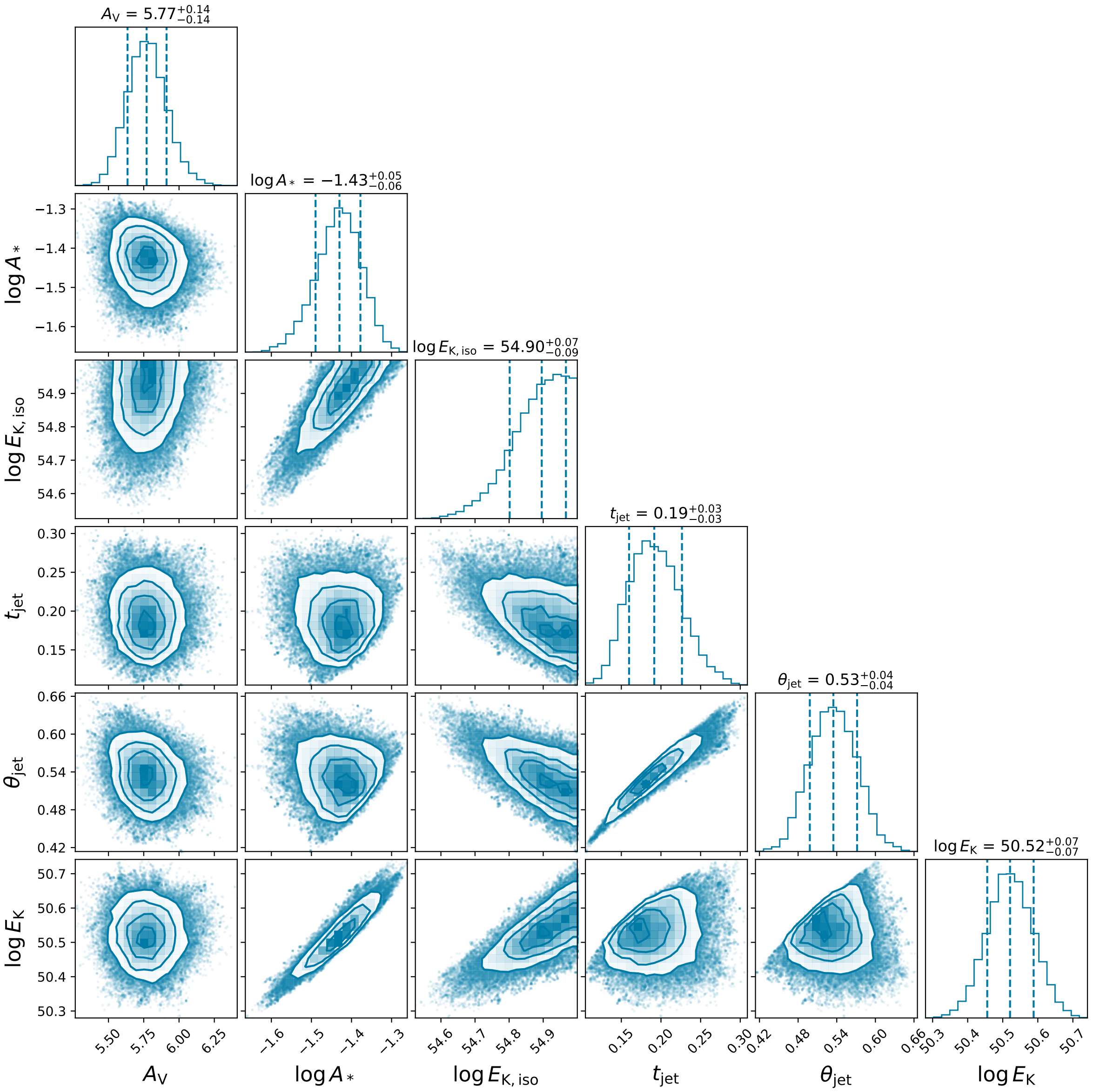

Figure 3. Results from modeling the multiwavelength X-ray, optical, and radio observations of GRB 250702B reported in A. J. Levan et al. (2025) with a standard GRB afterglow model.

Table 2
Results from Fits to Spectra Extracted Row by Row (Section 2.2)

Pixel Row	δz (10^{-4})	v (km s^{-1})	σ (nm)	$F_{\mathrm{Pa}\alpha}$ (10^{-18} erg s^{-1} cm^{-2})	$F_{\mathrm{H}\alpha}$	$F_{\mathrm{Br}\gamma}$ (10^{-19} erg s^{-1} cm^{-2})	A_V (mag)
30	28.2 ± 7.6	850 ± 230	11.2 ± 2.0	0.85 ± 0.13	1.22 ± 0.36	0.60 ± 0.50	2.88 ± 0.52
31	18.6 ± 3.5	560 ± 100	10.7 ± 0.8	2.02 ± 0.14	1.99 ± 0.33	1.78 ± 0.80	3.44 ± 0.28
32	−2.0 ± 3.0	−60 ± 90	11.8 ± 0.6	3.15 ± 0.17	2.54 ± 0.35	1.39 ± 0.84	3.76 ± 0.23
33	−22.6 ± 3.5	−680 ± 100	12.4 ± 0.7	3.01 ± 0.19	1.87 ± 0.35	3.34 ± 1.10	4.19 ± 0.33
34	−59.1 ± 4.2	−1780 ± 130	11.7 ± 1.0	2.22 ± 0.19	1.59 ± 0.35	3.74 ± 1.08	3.96 ± 0.38
35	−69.4 ± 6.6	−2400 ± 150	10.7 ±1.6	1.19 ± 0.17	1.08 ± 0.34	0.73 ± 0.62	3.58 ± 0.60

Note. Pixel numbers correspond to the spectra in Figure 2. The redshift offset δz is computed with respect to the systemic redshift derived from the integrated spectrum, $z = 1.036$, and velocities are $v = c\delta z$. Line fluxes are corrected for Galactic extinction but not for host extinction. A_V is calculated from case B recombination assuming an intrinsic ratio of $\mathrm{Pa}\alpha/\mathrm{H}\alpha = 0.122$ and a J. A. Cardelli et al. (1989) dust law with $R_V = 3.1$. The centroid of transient emission is expected in pixel row 32 (Section 2.2).

contribution, and the peak pixel contains ∼80% of the total SN flux. We redden the SN 2023lcr spectra by $A_V = 3.8$ as indicated by the galaxy spectrum (Table 2) and also by $A_V = 5.8$ as the implied line-of-sight extinction to the burst (Section 3.1 and Figure 3), using a J. A. Cardelli et al. (1989) extinction law with $R_V = 3.1$. Given that the extinction determination from the galaxy is set by the ensemble properties of the stellar population, we believe that the direct line-of-sight extinction determined from the afterglow is more likely to be relevant.

We note that the details of the subtraction limit are sensitive to the scaling of the host galaxy for subtraction. In particular, because of the heavy extinction, the spectral shapes expected for the SN and for the stellar population are similar, especially at low signal-to-noise ratio (S/N). Hence, some transient contribution cannot be excluded, although broad features comparable to SN 2023lcr are not visible in the subtraction (see Figure 2). For the low-extinction scenario the absence of these features is constraining, and we estimate that we would detect these features in subtractions to luminosities of 2–3 times fainter than AT2023lcr. However, since these are rest-frame optical/NIR features, they are substantially impacted by the additional dust in the higher-extinction scenario, and we could not identify SNe substantially fainter than AT2023lcr in this case.

As an orthogonal test of our sensitivity to an SN 2023lcr–like SN, we subtract decreasing fractions of the SN 2023lcr spectrum from the pixel 32 spectrum and measure whether the resulting flux deviations are greater or smaller than the measurement errors. This method is complementary to the host subtraction test because it essentially measures how faint an SN could be recovered with a "perfect" host subtraction. We subtract the reddened SN 2023lcr spectrum from pixel 32 (again using both $A_V = 3.8$ and $A_V = 5.8$) and divide the difference by the measurement uncertainties of the two original spectra added in quadrature. For $A_V = 3.8$, we find that for an SN with flux half that of SN 2023lcr the subtraction residuals are consistently between 2 and 5 times the measurement errors in the region between 1 and 3 μm (observed), while an SN 5× fainter than SN 2023lcr causes deviations barely in excess of 1σ in this interval. For the expected line-of-sight $A_V = 5.8$ from afterglow modeling, the subtraction residuals are at the 1σ level for an SN half the flux of SN 2023lcr and only reach 3σ for an equally bright SN. We therefore conclude that while we can exclude an SN of the same luminosity as SN 2023lcr, we cannot exclude SNe much fainter than it.

Ultimately, a second epoch of spectroscopy may reveal any transient light. Imaging observations also have the potential to identify such signatures, although we caution that with the heavy extinction it may be extremely difficult to use the properties of any transient observed only photometrically to place meaningful progenitor constraints.

3.3. Tidal Disruption Event Limits

A TDE from a supermassive black hole (SMBH) was strongly disfavored as the origin for GRB 250702B based on its off-nuclear position. We also note that the relatively flat optical–NIR SED of the jetted TDE AT2022cmc at an observed epoch of 41–46 days (D. R. Pasham et al. 2023) should produce a transient feature with extinction-corrected flux densities on the order of $\gtrsim 0.1$ μJy (for $A_V = 5.8$). While this SED was taken at $\sim$21 rest-frame days (compared to $\sim$25.5 for GRB 250702B), the light curve was relatively flat at this time ($t^{-0.3}$), and, at $z = 1.193$, AT2022cmc was also marginally more distant. The absence of an additional emission component in pixel 32 and adjacent rows therefore provides further evidence against a jetted TDE similar to AT2022cmc, although the diversity of optical/NIR emission in this population is not well-known.

The X-ray (0.5–4 keV) peak flux of GRB 250720B was measured by the EP Wide-field X-ray Telescope to be $(5.5 \pm 0.7) \times 10^{-10}$ erg cm^{-2} s^{-1} (H. Q. Cheng et al. 2025). With our redshift measurement, this converts to a peak (1.0–8.1 keV) X-ray luminosity of $L_{\rm X,peak} = 3 \times 10^{48}$ erg s^{-1}. This means that any nonrelativistic TDE scenario where the $L_{\rm X,peak}$ is not too far above the Eddington limit is ruled out (given that $L_{\rm X,peak}$ for even a black hole (BH) as massive as $10^8\,M_\odot$ would be $\approx 2 \times 10^{46}$ erg s^{-1}). Therefore, any TDE interpretation implies a strongly jetted (i.e., relativistic and Doppler-boosted) emission. This makes determining the mass from the BH responsible for the disruption uncertain, unlike for nonrelativistic TDEs, where the peak luminosity roughly scales with BH mass (E. Hammerstein et al. 2025). The timescale of the repeated gamma-ray detection is consistent with the orbital timescale of a white dwarf around an IMBH. Even for rapidly spinning BHs, the maximum mass of a BH able to tidally disrupt outside the event horizon will be $\lesssim 10^6$ $M_\odot$, thus in the not well-probed IMBH regime (see the review in K. Maguire et al. 2020).

Interestingly, another high-energy event (albeit in X-ray and not gamma-ray) was reported in P. G. Jonker et al. (2013). In that case, two precursor events with timescales of $\approx$4000 s were reported, and a similar scenario of a white dwarf IMBH TDE was envisaged. However, for that source no redshift determination was available, making the associated energy much more uncertain than for GRB 250702B. Deep host galaxy searches (D. Eappachen et al. 2022) did provide evidence for redshift scenarios that could imply a peak X-ray luminosity consistent with what we find for GRB 250702B.

4. Host Galaxy Properties

4.1. CIGALE Results

We modeled the GRB 250702B host galaxy using CIGALE (M. Boquien et al. 2019; D. Burgarella et al. 2025), in particular, its spectroscopic extension CIGALE-SPEC, which can simultaneously fit 1D spectrum and broadband photometry. We adopt a delayed star formation history with a recent burst component, motivated by the recent star formation activity typically observed in GRB host galaxies (S. Savaglio et al. 2009; T. Krühler et al. 2015). The age of the main stellar population is allowed to vary up to 5800 Myr, close to the maximum physically allowed at $z = 1.036$. For the burst component, we explore ages between 50 and 200 Myr, with mass fractions produced by the burst varying from 0 to 0.5. Stellar emission is modeled using the population synthesis models of G. Bruzual & S. Charlot (2003) with a Salpeter initial mass function (E. E. Salpeter 1955) and a metallicity set to $Z = 0.02$ (solar metallicity).

We included nebular emission with standard parameters and modeled dust attenuation using a modified version of the D. Calzetti et al. (2000) starburst attenuation law, with A_V allowed to vary between 2.5 and 8.5 to enclose the value derived from emission lines and afterglow modeling. The resulting best-fit model is shown in Table 3 and Figure 4. The model reproduces both the continuum shape and the Paα line flux well (model: $(10.3 \pm 0.1) \times 10^{-18}$ erg s^{-1} cm^{-2}) but underestimates the Hα flux (model: $(1.96 \pm 0.20) \times 10^{-18}$ erg s^{-1} cm^{-2}) by a factor of $\sim$5. This discrepancy may reflect local variations in

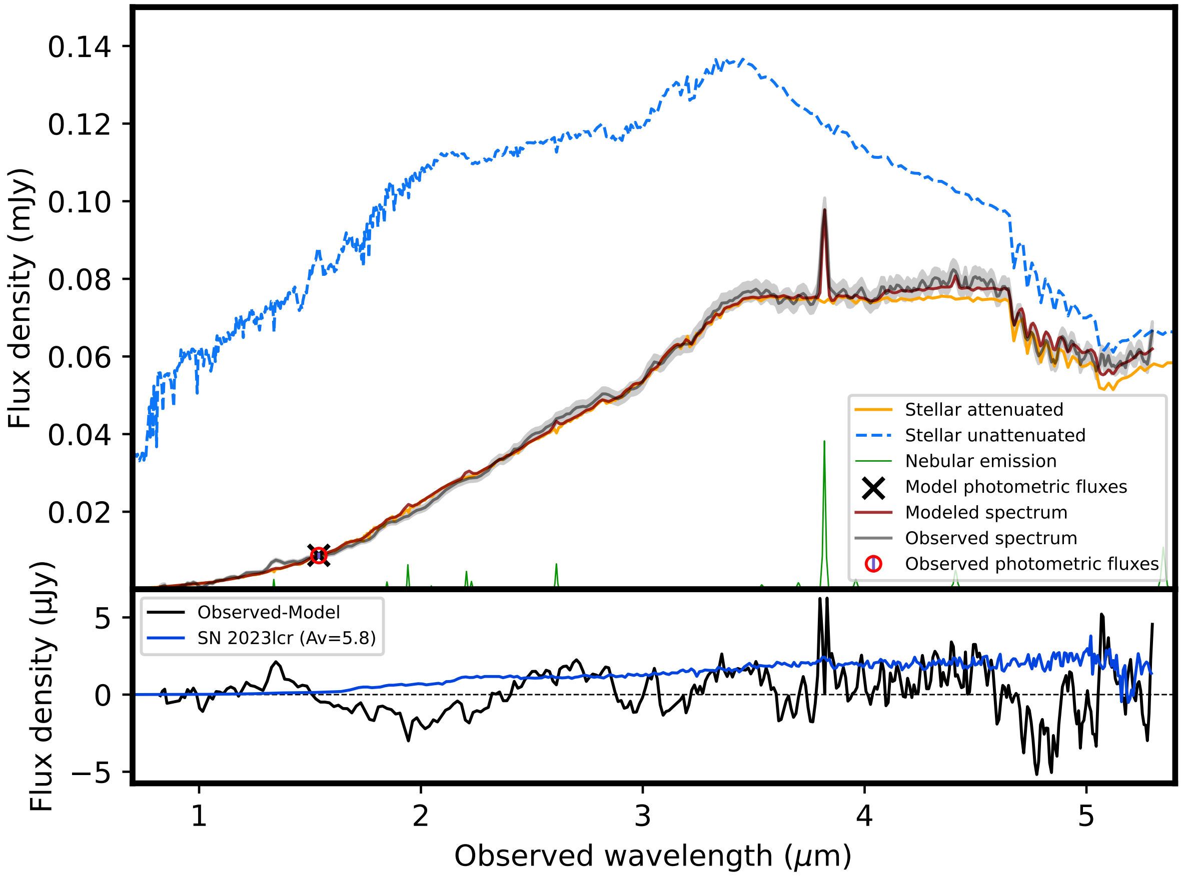

Figure 4. Best-fit model for the GRB 250702B host galaxy obtained with CIGALE. The observed spectrum is shown as a gray curve, and the HST/WFC3 F160W photometric point is shown as a red circle. The resulting best-fit model is plotted in red, with the corresponding model photometric flux indicated by a black cross. The contributions from the attenuated stellar continuum (orange), intrinsic unattenuated stellar emission (blue), and nebular emission (green) are shown separately. The bottom panel displays the difference between the observed and best-fit model spectrum (black), as well as SN 2023lcr (blue) as it would appear with $A_V = 5.8$. The inferred parameters are given in Table 3.

Table 3
The Properties of GRB 250702B's Host Galaxy Inferred from Spectral Fitting, as Outlined in Section 4

Parameter	CIGALE
$\log_{10}(M_*/M_\odot)$	$11.60^{+0.14}_{-0.14}$
$t_{\rm age}$ (Gyr)	4.9 ± 0.6
τ (Gyr)	$0.550^{+0.180}_{-0.180}$
A_V (mag)	6.2 ± 0.1
SFR ($M_\odot$ yr^{-1})	93 ± 11

Note. Median a posteriori parameter values are given, with uncertainties bounding 68% confidence intervals. Since the spectrum was scaled to match the host-integrated F160W HST measurement, the values below assume that the portion of the galaxy in the slit is representative of the stellar population throughout the host.

dust attenuation that suppress optical nebular emission more strongly than in the NIR and are not fully captured by the simple attenuation prescription adopted in our modeling. Alternatively, it may suggest that the Hα line originates from a physical mechanism not captured by the recent star formation component modeled by CIGALE-SPEC.

The Bayesian analysis indicates a main stellar population age of 4.9 ± 0.6 Gyr, with an *e*-folding timescale of $\tau_{\rm main} = (550 \pm 180)$ Myr. A recent burst component is favored, with a characteristic age of 129 ± 46 Myr and a mass fraction of $f_{\rm burst} = 0.050 \pm 0.004$, consistent with recent star formation activity. The model implies a dust attenuation corresponding to $E(B-V)_{\rm lines} = 2.0 \pm 0.1$, i.e., a nebular $A_V = (6.2 \pm 0.1)$ mag, consistent with the afterglow-derived value. The host has a stellar mass of $\log_{10}(M_\star/M_\odot) = 11.60 \pm 0.14$ and a star formation rate (SFR) of $\log_{10}({\rm SFR}/M_\odot\ {\rm yr}^{-1}) = 1.97 \pm 0.05$ (SFR $=93 \pm 11\ M_\odot$ yr^{-1}), placing it on or above the star-forming main sequence at $z \approx 1$ (C. Schreiber et al. 2015). We note that our spectrum samples only a limited portion of the host galaxy (Figure 1). To approximate the integrated properties, we use the Hubble Space Telescope (HST)/WFC3 F160W magnitude reported in A. J. Levan et al. (2025) to normalize the spectrum and extrapolate the results returned by CIGALE-SPEC to the whole galaxy. However, the slit placement was not arbitrary and was not centered on the brightest regions of the system. Consequently, this normalization may yield a stellar mass and SFR that are not fully representative of the global galaxy properties. Additional photometric data, particularly in the infrared, are required to more robustly constrain and characterize the host. In the bottom panel of Figure 4, we show the residual spectrum obtained by subtracting the best-fit model from the data. As in Section 3.2, we compare these residuals to a reddened ($A_V = 5.8$) spectrum of SN 2023lcr to search for possible contamination from a transient. Complementary to Section 3.2, this analysis does not support the presence of residual light from a transient at least as bright as SN 2023lcr.

4.2. Star Formation Rate from Balmer and Paschen Lines

We independently estimated the SFR from the observed Balmer and Paschen line fluxes using the equation scaled for solar metallicity in N. A. Reddy et al. (2023). After correcting the fluxes reported in Table 1 for host extinction with $A_V = 3.1$ mag, we derive $\mathrm{SFR}_{\mathrm{Pa}\alpha} = 14.7 \pm 1.1\, M_\odot\, \mathrm{yr}^{-1}$ and $\mathrm{SFR}_{\mathrm{H}\alpha} = 7.0 \pm 1.1\, M_\odot\, \mathrm{yr}^{-1}$. As Pa$\alpha$ is less affected by dust attenuation than Hα, its derived SFR is expected to exceed that from Hα. A factor up to ~2 difference was observed in N. A. Reddy et al. (2023). The much larger SFR inferred from the SED fitting is explained by the normalization factor applied (approximately ×10), which is not used in the line-based estimates. Given that only a small fraction of the galaxy was covered by the NIRSpec slit and the high A_V exhibited by the host, which may still affect the Paα line, these SFRs should be considered as lower limits on the total SFR of the galaxy.

4.3. Identified Absorption Features

The CO first-overtone band head is reproduced within the CIGALE code, and this provides a direct perspective on the stellar population (e.g., R. Doyon et al. 1994; L. Origlia & E. Oliva 2000; A. Mármol-Queraltó et al. 2008). In particular, this feature originates in cool stellar atmospheres and can therefore arise from red supergiants in starbursts galaxies, asymptotic giant branch stars at intermediate ages, and the K/M-type giants that dominate older populations. The modest strength of the CO molecular band with $D_{\mathrm{CO}} \sim 1.15$ (e.g., the fractional decrease of the continuum flux measured at the CO 2–0 absorption following the definition in A. Mármol-Queraltó et al. 2008) suggests that the integrated light is dominated by stars with effective temperatures of ~4000 K. This interpretation is further strengthened by the likely presence of H_2O molecular absorption, which is also expected in the cool atmospheres of late-type stars (e.g., A. Lançon & P. R. Wood 2000).

5. Discussion

5.1. Rates and $E_{\gamma,iso}$ in Context

Combining our measured redshift of $z = 1.036$ with the fluence measured by Konus-Wind (D. Frederiks et al. 2025), we infer an isotropic-equivalent γ-ray energy release of $E_{\gamma,\mathrm{iso}} = (1.8 \pm 0.1) \times 10^{54}$ erg (corresponding to a prompt efficiency of $\eta_\gamma \approx 20\%$; Section 3.1). To properly compare this to GRBs at a range of redshifts, a cosmological K-correction must be applied to account for the shifting rest-frame bandpass (see J. S. Bloom et al. 2001). The best-fit spectrum for the time-integrated Konus-Wind (R. L. Aptekar et al. 1995) observations was a power law with a photon index of $\Gamma = 1.30 \pm 0.06$ in the energy range 20–1250 keV. GRB $E_{\gamma,\mathrm{iso}}$ values are typically K-corrected to a bolometric rest-frame bandpass of 1 keV–10 MeV (e.g., A. Tsvetkova et al. 2017, 2021; E. Burns et al. 2023). This results in a K-corrected $E_{\gamma,\mathrm{iso}} = 8.2 \times 10^{54}$ erg. This would make GRB 250702B the second most energetic GRB of all time, behind only GRB 221009A (the "BOAT"; E. Burns et al. 2023). However, this is in part because the νF_ν peak of the spectrum is above the observed bandpass, making the energy solution unbound (i.e., tending to infinity as the bandpass increases). Assuming a peak energy of 1500 keV (just above the measured energy range) gives $E_{\gamma,\mathrm{iso}} = 2.2 \times 10^{54}$ erg, placing GRB 250702B just below the 15 GRBs with $E_{\gamma,\mathrm{iso}} > 2.5 \times 10^{54}$ erg presented in E. Burns et al. (2023) in energy output. We note that the $E_{\gamma,\mathrm{iso}}$ calculated here is a lower limit, since related X-ray emission of an unreported duration was observed to emerge the day before the first Fermi/GBM trigger by EP (H. Q. Cheng et al. 2025).

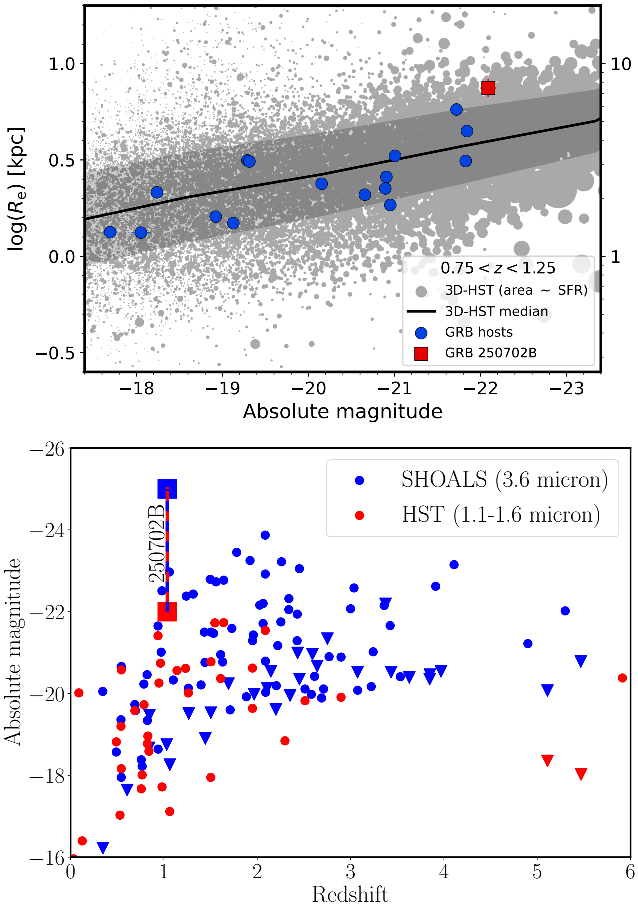

Figure 5. Top*:* half-light radius (R_e) as a function of F160W (~H-band) observed absolute magnitude for GRB host galaxies and 3D-HST star-forming galaxies at $0.75 < z < 1.25$. The red square marks the host galaxy of GRB 250702B. Blue circles show other GRB host galaxies, while gray circles represent star-forming galaxies, with their area scaled to the SFR. The black line indicates the median relation for the star-forming population, and the light-gray shaded region shows its 1σ scatter. Bottom: redshift vs. absolute magnitude for GRB hosts across a wider redshift range. The host of GRB 250702B is the most luminous GRB host observed to date in both the near-IR and (likely) the mid-IR.

We also estimate the rarity of events like GRB 250702B. Taking it as a singular event in the Fermi/GBM catalog, which began in 2009 (D. Gruber et al. 2014; A. von Kienlin et al. 2014; P. Narayana Bhat et al. 2016; A. von Kienlin et al. 2020), gives a time baseline of 16 yr. To estimate the search volume, we take the least significant of the three subevents, originally designated as GRB 250702D (Fermi GBM Team 2025), and calculate the maximum distance from which the burst could have been detected. The General Coordinates Network (GCN) notice associated with this event indicates that it was detected in flight with a significance of 5.1σ in the 4.096 s time bin. The Fermi/GBM triggering algorithm requires a significance[31] of 4.5σ in two detectors; hence, with our measured distance of 7.1 Gpc, GRB 250702D

---

[31] https://fermi.gsfc.nasa.gov/science/resources/swg/bwgreview/Trigger_Algorithms.pdf

could have been detected from a maximum distance of $D_{\rm max} = 7.1/\sqrt{4.5/5.1} = 7.6$ Gpc. The detection rate can therefore be approximated as $R_{\rm det} = 5 \times 10^{-4}\,{\rm yr}^{-1}\,{\rm Gpc}^{-3}$. Corrected for the very narrow jet found in afterglow modeling (Section 3.1) and assuming a "top-hat" jet, the true volumetric event rate is $R_{\rm evt} = R_{\rm det}/(1 - \cos(\theta_{\rm jet})) = 11\,{\rm yr}^{-1}\,{\rm Gpc}^{-3}$. This is approximately 10^{-5} times the estimated rate of core-collapse SNe out to a similar redshift (T. Dahlen et al. 2012) and, before correction for beaming, is a factor of $>10^3$ lower than the implied rate for high-luminosity long GRBs (H. Sun et al. 2015).

The above calculations are clearly simplified, neglecting occulted regions of the sky, variable sensitivity and background rates, and the impact redshifting has on received counts when observing with a fixed bandpass (e.g., O. M. Littlejohns et al. 2013), among other factors. Nonetheless, with no comparable events in the archive, the true event rate is clearly low. We leave a full treatment of these factors to future work.

5.2. Limits on the Exclusion of an Associated Supernova

To date we have observed more than 60 GRB-SN associations, with almost half of them spectroscopically confirmed (e.g., Z. Cano et al. 2017; G. Finneran et al. 2025b). The properties of these Type Ic-BL GRB-SNe are remarkably similar in all cases, with similar spectroscopic features and evolutions (G. Finneran et al. 2025a). Their light curves show narrow distributions in both the quasi-bolometric light-curve parameter $k_{\rm bol}$ and the quasi-bolometric stretch factor $s_{\rm bol}$ (e.g., S. Klose et al. 2019), signaling similar peak luminosities (within a factor of 3–5×) with respect to the archetypal GRB-SN, SN 1998bw, and similar progenitor stars. The derived limit suggests the possibility of an undetected SN component associated with GRB 250702B with similar luminosity to SN 2023lcr, which is, in terms of its peak magnitude, released mass of radioactive nickel, kinetic energy, and ejected mass, an average case within the GRB-SN population (see, e.g., Z. Cano et al. 2017; G. Finneran et al. 2025b, for the range of values typically seen in GRB-SN associations for these parameters). Thus, this limit only allows us to rule out the top ∼40% most powerful GRB-SN cases, such as SN 1998bw (e.g., T. J. Galama et al. 1998), SN 2010ma (e.g., M. Sparre et al. 2011), SN 2012bz (e.g., S. Schulze et al. 2014), and SN 2011kl (e.g., B. Gendre et al. 2013), among others. Furthermore, if GRB-less Type Ic-BL SNe and other types of stripped-enveloped SNe (such as Types Ic, Ib, and IIb) are considered as potential associations with GRB 250702B (pointing toward a different progenitor), the luminosity limit would be even less restricting than in the GRB-SN scenario (e.g., J. D. Lyman et al. 2016; N. Afsariardchi et al. 2021), leaving these alternative progenitor scenarios still open.

5.3. Galaxy Context

We compare the galaxy size (half-light radius, R_e) and absolute magnitude of the GRB 250702B host galaxy, as measured by A. J. Levan et al. (2025), with those of field star-forming galaxies at similar redshifts. Figure 5 shows the half-light radius as a function of observed absolute magnitude in the HST/WFC3 F160W (approximately H-band) filter for GRB host galaxies from P. K. Blanchard et al. (2016) and for star-forming galaxies drawn from the 3D-HST survey (G. B. Brammer et al. 2012; R. E. Skelton et al. 2014; A. van der Wel et al. 2014; I. G. Momcheva et al. 2016) within $z \pm 0.25$. The host galaxy of GRB 250702B (red square) lies significantly above the median size–luminosity relation of the field population and is located at the bright, large end of the star-forming galaxy distribution. GRB host galaxies at these redshifts are typically star-forming, metal-poor, compact, and dense systems (A. S. Fruchter et al. 2006; P. L. Kelly et al. 2014; J. Japelj et al. 2016; J. T. Palmerio et al. 2019; B. Schneider et al. 2022). More massive, dustier, and near-supersolar-metallicity hosts are rarer but have been reported (e.g., E. M. Levesque et al. 2010; P. Schady et al. 2015; D. A. Perley et al. 2016). The GRB 250702B host stands out as one of the brightest and most extended known at this redshift range, indicating a relatively unusually massive and evolved system within the GRB host population.

In terms of morphology, the host has concentration and asymmetry (C. J. Conselice et al. 2005) values of $C = 1.88$ and $A = 0.059$ (measured on the HST F160W image with STATMORPH; V. Rodriguez-Gomez et al. 2019). This is a typical asymmetry for GRB hosts. The concentration parameter, on the other hand, is among the lowest ever measured in the GRB host population (J. D. Lyman et al. 2017; A. A. Chrimes et al. 2019) and reflects the galaxy's highly extended nature outside the two prominent bright regions.

We further compare the properties of the host of GRB 250702B with the GRB host population across a wider range of redshift in Figure 5. Comparison to the near-IR observations is undertaken directly with the HST integrated host measurement. To estimate the comparison to the much larger sample taken as part of the SHOALS survey (D. A. Perley et al. 2016), we first estimate the color based on that observed with NIRSPEC and then apply the same normalization from the NIRSPEC slit to the integrated light as used in the H band. This is reasonable since there are not large color gradients within our data, although there is a slight trend to redder colors nearer the galaxy nucleus. From this it is apparent that in both the near-IR (rest-frame) optical and mid-IR the host of GRB 250702B is the most luminous GRB host to date. Given the combination of exceptional burst and exceptional host, it is tempting to speculate whether the two are related.

ERIS imaging shows GRB 250702B to lie in close proximity to structure in the host galaxy, which may well be related to the emission-line structures seen in the JWST spectroscopy. This indicates that the GRB did not come from the center of mass of any large structure, although the emission lines are at their brightest at the burst location. The extended nature of these lines and the fact that the burst does not lie at an apparent peak of the light within the host may disfavor an IMBH TDE from the higher end of the IMBH mass function, which may be expected to dominate its local environment. The galaxy is apparently dominated by an old stellar population, which could imply an unusual channel. However, there is also evidence for significant star formation, in particular at the burst position, indicating that an SN origin remains plausible. The very high mass of the galaxy in principle should yield a high metallicity, although robust metallicity estimates cannot be obtained from our spectroscopy. If this is the case, standard collapsar models may struggle to explain the burst, although more exotic scenarios may be possible, especially given the rarity of events like GRB 250702B.

6. Conclusions

We performed follow-up observations of the exceptional repeating GRB 250702B with JWST/NIRSpec and VLT/ERIS. Our spectroscopic observations reveal the redshift of the GRB to be $z = 1.036 \pm 0.004$, which places a lower limit of $E_{\gamma\mathrm{iso}} > 2.2 \times 10^{54}$ erg, assuming a conservative νF_ν peak energy of 1500 keV and neglecting additional flux detected in X-rays by EP starting the day prior to the Fermi/GBM triggers. This places GRB 250702B among the very brightest GRBs in the observed catalog, though its extremely narrow jet opening angle inferred from afterglow modeling would result in more typical beaming-corrected GRB energies (e.g., D. A. Frail et al. 2001).

The host galaxy of GRB 250702B is one of the intrinsically brightest and most spatially extended in the HST and SHOALS samples, particularly at 3.6 μm, where it is almost a magnitude brighter than any other GRB host in absolute terms. The dominant stellar population in the region close to the GRB is found to be 4.9 ± 0.6 Gyr old, although modeling with CIGALE favors the inclusion of a burst component with a characteristic age of 129 ± 46 Myr, indicating that ≈5% of the stellar mass comes from recent star formation. The SFR itself is typical for a galaxy of this size and at this redshift. The galaxy is extremely dusty, with A_V measurements ranging from $A_V = 3.8 \pm 0.2$ from Paα-to-Hα line ratios from the spectrum covering the GRB position, to $A_V = 3.4 \pm 0.4$ from the same line ratios in the spatially integrated 1D NIRSpec spectrum, to $A_V = 5.8 \pm 0.1$ along the GRB line of sight from afterglow modeling, to $A_V = 6.2 \pm 0.1$ from galaxy modeling.

Despite the extremely high visual extinction of the host, we are able to exclude the presence of a typical GRB-SN with a luminosity comparable to SN 2023lcr. However, our observations are only constraining to the brightest 40% of known GRB-SNe and are not sensitive to other SN types. We are therefore unable to exclude a stellar collapse origin for GRB 250702B. We are also not able to constrain the presence of an IMBH TDE, although the observed position of the GRB is offset from the brightest regions of nearby star formation, indicating that it did not come from the center of a local mass structure as might be expected for BHs on the higher end of the IMBH mass spectrum.

Our observations have confirmed GRB 250702B to be a surprisingly distant event given the observed brightness of its host galaxy. The associated energy release is enough to strain, but not definitely break, canonical GRB collapsar models. If it is a collapsar, we estimate it to be a 1-in-1000 event in the high-luminosity GRB population. The beaming-corrected event rate suggests that it must come from a progenitor more than 10^5 times rarer than core-collapse SNe. Ultimately, follow-up spectroscopic observations may help to reveal transient light in the spectra presented here that is obfuscated by the extremely dusty sight line to the burst and to elucidate the progenitor of this rare, powerful, and surprisingly distant relativistic transient.

Acknowledgments

This work is based in part on observations made with the NASA/ESA/CSA James Webb Space Telescope. The data were obtained from the Mikulski Archive for Space Telescopes at the Space Telescope Science Institute, which is operated by the Association of Universities for Research in Astronomy, Inc., under NASA contract NAS 5-03127 for JWST. These observations are associated with program Nos. 4554 and 9254. This work is based on observations made with the NASA/ESA Hubble Space Telescope. These observations are associated with program No. 17988. Based on observations collected at the European Southern Observatory under ESO program(s) 114.27PZ.

This work is based in part on observations taken by the 3D-HST Treasury Program (GO 12177 and 12328) with the NASA/ESA HST, which is operated by the Association of Universities for Research in Astronomy, Inc., under NASA contract NAS5-26555.

B.P.G. and Dimple acknowledge support from STFC grant No. ST/Y002253/1. B.P.G. and D.O. acknowledge support from the Leverhulme Trust grant No. RPG-2024-117. B.S. acknowledges the support of the French Agence Nationale de la Recherche (ANR), under grant ANR-23-CE31-0011 (project PEGaSUS). A.A.C. acknowledges support through the European Space Agency (ESA) research fellowship program. A.Sn and D.B.M. are funded by the European Union (ERC, HEAVYMETAL, 101071865). P.G.J. and M.E.R. are funded by the European Union (ERC, Starstruck, 101095973). Views and opinions expressed are, however, those of the authors only and do not necessarily reflect those of the European Union or the European Research Council Executive Agency. Neither the European Union nor the granting authority can be held responsible for them. A.M.C. and L.C. acknowledge support from the Irish Research Council Postgraduate Scholarship No. GOIPG/2022/1008. The Cosmic Dawn Center (DAWN) is funded by the Danish National Research Foundation under grant DNRF140. L.I. acknowledges financial support from the INAF Data Grant Program "YES" (PI: Izzo) *Multi-wavelength and multi messenger analysis of relativistic supernovae*. G.P.L. is supported by a Royal Society Dorothy Hodgkin Fellowship (grant Nos. DHF-R1-221175 and DHF-ERE-221005). A.Sa acknowledges support by a postdoctoral fellowship from the CNES. M.E.W. is supported by the Science and Technology Facilities Council (STFC). N.R.T. acknowledges support from STFC grant ST/W000857/1.

We thank V. Buat and D. Burgarella for the useful discussions regarding the CIGALE SED fitting.

Software: `Astropy` (Astropy Collaboration et al. 2013, 2018, 2022); CIGALE (M. Boquien et al. 2019; D. Burgarella et al. 2025); `extinction` (K. Barbary 2016); `jwst` pipeline (H. Bushouse et al. 2022); REFLEX pipeline (W. Freudling et al. 2013).

ORCID iDs

Benjamin P. Gompertz https://orcid.org/0000-0002-5826-0548
Andrew J. Levan https://orcid.org/0000-0001-7821-9369
Tanmoy Laskar https://orcid.org/0000-0003-1792-2338
Benjamin Schneider https://orcid.org/0000-0003-4876-7756
Ashley A. Chrimes https://orcid.org/0000-0001-9842-6808
Antonio Martin-Carrillo https://orcid.org/0000-0001-5108-0627
Albert Sneppen https://orcid.org/0000-0002-5460-6126
David O'Neill https://orcid.org/0009-0001-1554-1868
Daniele B. Malesani https://orcid.org/0000-0002-7517-326X
Peter G. Jonker https://orcid.org/0000-0001-5679-0695

Eric Burns https://orcid.org/0000-0002-2942-3379
Gregory Corcoran https://orcid.org/0009-0009-1573-8300
Laura Cotter https://orcid.org/0000-0002-7910-6646
Antonio de Ugarte Postigo https://orcid.org/0000-0001-7717-5085
Massimiliano De Pasquale https://orcid.org/0000-0002-4036-7419
Dimple https://orcid.org/0000-0001-9868-9042
Rob A. J. Eyles-Ferris https://orcid.org/0000-0002-8775-2365
Andrew Fruchter https://orcid.org/0000-0002-6652-9279
Luca Izzo https://orcid.org/0000-0001-9695-8472
Páll Jakobsson https://orcid.org/0000-0002-9404-5650
Gavin P. Lamb https://orcid.org/0000-0001-5169-4143
Jesse T. Palmerio https://orcid.org/0000-0002-9408-1563
Giovanna Pugliese https://orcid.org/0000-0003-3457-9375
Maria Edvige Ravasio https://orcid.org/0000-0003-3193-4714
Andrea Saccardi https://orcid.org/0000-0002-6950-4587
Ruben Salvaterra https://orcid.org/0000-0002-9393-8078
Nikhil Sarin https://orcid.org/0000-0003-2700-1030
Steve Schulze https://orcid.org/0000-0001-6797-1889
Nial Tanvir https://orcid.org/0000-0003-3274-6336
Isabelle Worssam https://orcid.org/0009-0007-3476-2272
Makenzie E. Wortley https://orcid.org/0009-0009-8473-3407

References

Afsariardchi, N., Drout, M. R., Khatami, D. K., et al. 2021, ApJ, 918, 89
Andreoni, I., Coughlin, M. W., Perley, D. A., et al. 2022, Natur, 612, 430
Aptekar, R. L., Frederiks, D. D., Golenetskii, S. V., et al. 1995, SSRv, 71, 265
Astropy Collaboration, Price-Whelan, A. M., Lim, P. L., et al. 2022, ApJ, 935, 167
Astropy Collaboration, Price-Whelan, A. M., Sipőz, B. M., et al. 2018, AJ, 156, 123
Astropy Collaboration, Robitaille, T. P., Tollerud, E. J., et al. 2013, A&A, 558, A33
Barbary, K. 2016, extinction v0.3.0, v1, Zenodo, doi: 10.5281/zenodo.804967
Bennett, C. L., Larson, D., Weiland, J. L., & Hinshaw, G. 2014, ApJ, 794, 135
Blanchard, P. K., Berger, E., & Fong, W.-f. 2016, ApJ, 817, 144
Bloom, J. S., Frail, D. A., & Sari, R. 2001, AJ, 121, 2879
Boquien, M., Burgarella, D., Roehlly, Y., et al. 2019, A&A, 622, A103
Brammer, G. B., van Dokkum, P. G., Franx, M., et al. 2012, ApJS, 200, 13
Bruzual, G., & Charlot, S. 2003, MNRAS, 344, 1000
Burgarella, D., van Dokkum, P. G., Franx, M., et al. 2025, A&A, 699, A336
Burns, E., Svinkin, D., Fenimore, E., et al. 2023, ApJL, 946, L31
Burrows, D. N., Kennea, J. A., Ghisellini, G., et al. 2011, Natur, 476, 421
Bushouse, H., Eisenhamer, J., Dencheva, N., et al. 2022, JWST Calibration Pipeline, v1.7.0, Zenodo
Calzetti, D., Armus, L., Bohlin, R. C., et al. 2000, ApJ, 533, 682
Cano, Z., Wang, S.-Q., Dai, Z.-G., & Wu, X.-F. 2017, AdAst, 2017, 8929054
Cardelli, J. A., Clayton, G. C., & Mathis, J. S. 1989, ApJ, 345, 245
Cenko, S. B., Krimm, H. A., Horesh, A., et al. 2012, ApJ, 753, 77
Cheng, H. Q., Zhao, G. Y., Zhou, C., et al. 2025, GCN, 40906, 1
Chrimes, A. A., Levan, A. J., Stanway, E. R., et al. 2019, MNRAS, 486, 3105
Conselice, C. J., Vreeswijk, P. M., Fruchter, A. S., et al. 2005, ApJ, 633, 29
Dahlen, T., Strolger, L.-G., Riess, A. G., et al. 2012, ApJ, 757, 70
Doyon, R., Joseph, R. D., & Wright, G. S. 1994, ApJ, 421, 101
Eappachen, D., Jonker, P. G., Fraser, M., et al. 2022, MNRAS, 514, 302
Fermi GBM Team 2025, GCN, 40886, 1
Finneran, G., Cotter, L., & Martin-Carrillo, A. 2025a, A&A, 700, A200
Finneran, G., Cotter, L., & Martin-Carrillo, A. 2025b, A&C, 52, 100954
Foreman-Mackey, D., Hogg, D. W., Lang, D., & Goodman, J. 2013, PASP, 125, 306
Frail, D. A., Kulkarni, S. R., Sari, R., et al. 2001, ApJL, 562, L55
Frederiks, D., Lysenko, A., Ridnaia, A., et al. 2025, GCN, 40914, 1
Freudling, W., Romaniello, M., Bramich, D. M., et al. 2013, A&A, 559, A96
Fruchter, A. S., Levan, A. J., Strolger, L., et al. 2006, Natur, 441, 463
Fynbo, J. P. U., Watson, D., Thöne, C. C., et al. 2006, Natur, 444, 1047
Galama, T. J., Vreeswijk, P. M., van Paradijs, J., et al. 1998, Natur, 395, 670
Gal-Yam, A., Fox, D. B., Price, P. A., et al. 2006, Natur, 444, 1053
Gehrels, N., Norris, J. P., Barthelmy, S. D., et al. 2006, Natur, 444, 1044
Gendre, B., Stratta, G., Atteia, J. L., et al. 2013, ApJ, 766, 30
Gompertz, B. P., Ravasio, M. E., Nicholl, M., et al. 2023, NatAs, 7, 67
Gruber, D., Goldstein, A., Weller von Ahlefeld, V., et al. 2014, ApJS, 211, 12
Hammerstein, E., Cenko, S. B., Andreoni, I., et al. 2025, arXiv:2506.08250
Hjorth, J., Sollerman, J., Møller, P., et al. 2003, Natur, 423, 847
Japelj, J., Vergani, S. D., Salvaterra, R., et al. 2016, A&A, 590, A129
Jonker, P. G., Glennie, A., Heida, M., et al. 2013, ApJ, 779, 14
Kelly, P. L., Filippenko, A. V., Modjaz, M., & Kocevski, D. 2014, ApJ, 789, 23
Klose, S., Schmidl, S., Kann, D. A., et al. 2019, A&A, 622, A138
Krühler, T., Malesani, D., Fynbo, J. P. U., et al. 2015, A&A, 581, A125
Lançon, A., & Wood, P. R. 2000, A&AS, 146, 217
Laskar, T., Berger, E., Margutti, R., et al. 2015, ApJ, 814, 1
Levan, A. J., Gompertz, B. P., Salafia, O. S., et al. 2024, Natur, 626, 737
Levan, A. J., Martin-Carrillo, A., Laskar, T., et al. 2025, ApJL, 990, L28
Levan, A. J., Tanvir, N. R., Brown, G. C., et al. 2016, ApJ, 819, 51
Levan, A. J., Tanvir, N. R., Starling, R. L. C., et al. 2014, ApJ, 781, 13
Levesque, E. M., Kewley, L. J., Graham, J. F., & Fruchter, A. S. 2010, ApJL, 712, L26
Littlejohns, O. M., Tanvir, N. R., Willingale, R., et al. 2013, MNRAS, 436, 3640
Lyman, J. D., Bersier, D., James, P. A., et al. 2016, MNRAS, 457, 328
Lyman, J. D., Levan, A. J., Tanvir, N. R., et al. 2017, MNRAS, 467, 1795
Maguire, K., Eracleous, M., Jonker, P. G., MacLeod, M., & Rosswog, S. 2020, SSRv, 216, 39
Mangano, V., Burrows, D. N., Sbarufatti, B., & Cannizzo, J. K. 2016, ApJ, 817, 103
Mármol-Queraltó, A., Cardiel, N., Cenarro, A. J., et al. 2008, A&A, 489, 885
Martin-Carrillo, A., Levan, A. J., de Ugarte Postigo, A., et al. 2023, GCN, 34385, 1
Martin-Carrillo, A., Schneider, B., Pugliese, G., et al. 2024, GCN, 37293, 1
Meegan, C., Lichti, G., Bhat, P. N., et al. 2009, ApJ, 702, 791
Momcheva, I. G., Brammer, G. B., van Dokkum, P. G., et al. 2016, ApJS, 225, 27
Narayana Bhat, P., Meegan, C. A., von Kienlin, A., et al. 2016, ApJS, 223, 28
Neights, E., Roberts, O. J., Burns, E., et al. 2025, GCN, 40931, 1
Oganesyan, G., Kammoun, E., Ierardi, A., et al. 2025, A&A, 703, L2
Origlia, L., & Oliva, E. 2000, A&A, 357, 61
Palmerio, J. T., Vergani, S. D., Salvaterra, R., et al. 2019, A&A, 623, A26
Pasham, D. R., Cenko, S. B., Levan, A. J., et al. 2015, ApJ, 805, 68
Pasham, D. R., Lucchini, M., Laskar, T., et al. 2023, NatAs, 7, 88
Perley, D. A., Andreoni, I., El-Badry, K., et al. 2023, GCN, 34041, 1
Perley, D. A., Tanvir, N. R., Hjorth, J., et al. 2016, ApJ, 817, 8
Rastinejad, J. C., Gompertz, B. P., Levan, A. J., et al. 2022, Natur, 612, 223
Reddy, N. A., Topping, M. W., Sanders, R. L., Shapley, A. E., & Brammer, G. 2023, ApJ, 948, 83
Rodriguez-Gomez, V., Snyder, G. F., Lotz, J. M., et al. 2019, MNRAS, 483, 4140
Salpeter, E. E. 1955, ApJ, 121, 161
Savaglio, S., Glazebrook, K., & Le Borgne, D. 2009, ApJ, 691, 182
Schady, P., Krühler, T., Greiner, J., et al. 2015, A&A, 579, A126
Schlafly, E. F., & Finkbeiner, D. P. 2011, ApJ, 737, 103
Schneider, B., Le Floc'h, E., Arabsalmani, M., Vergani, S. D., & Palmerio, J. T. 2022, A&A, 666, A14
Schreiber, C., Pannella, M., Elbaz, D., et al. 2015, A&A, 575, A74
Schroeder, G., Laskar, T., Fong, W.-f., et al. 2022, ApJ, 940, 53
Schulze, S., Malesani, D., Cucchiara, A., et al. 2014, A&A, 566, A102
Skelton, R. E., Whitaker, K. E., Momcheva, I. G., et al. 2014, ApJS, 214, 24
Sparre, M., Sollerman, J., Fynbo, J. P. U., et al. 2011, ApJL, 735, L24
Stanek, K. Z., Matheson, T., Garnavich, P. M., et al. 2003, ApJL, 591, L17
Sun, H., Zhang, B., & Li, Z. 2015, ApJ, 812, 33
Tenenbaum, E. D., Clayton, G. C., Asplund, M., et al. 2005, AJ, 130, 256
Tikhomirova, Y. Y., & Stern, B. E. 2005, AstL, 31, 291
Troja, E., Fryer, C. L., O'Connor, B., et al. 2022, Natur, 612, 228
Tsvetkova, A., Frederiks, D., Golenetskii, S., et al. 2017, ApJ, 850, 161
Tsvetkova, A., Frederiks, D., Svinkin, D., et al. 2021, ApJ, 908, 83
van der Wel, A., Franx, M., van Dokkum, P. G., et al. 2014, ApJ, 788, 28
Virgili, F. J., Mundell, C. G., Pal'shin, V., et al. 2013, ApJ, 778, 54
von Kienlin, A., Meegan, C. A., Paciesas, W. S., et al. 2014, ApJS, 211, 13
von Kienlin, A., Meegan, C. A., Paciesas, W. S., et al. 2020, ApJ, 893, 46
Yang, Y.-H., Troja, E., O'Connor, B., et al. 2024, Natur, 626, 742